metals

Article

Effect of Precipitates on Dislocation Loops in Vanadium Alloy After Irradiation with 60 keV Deuterium Ions at Room Temperature

Jing Wang [1,2], Mingxin Chen [1], Yifan Zhang [1,2,*], Bing Ma [1,2], Haiyan Jiang [1,3] and Chang Chen [2]

[1] School of Materials Science and Engineering, Hefei University of Technology, Hefei 230009, China; jwang@hfut.edu.cn (J.W.); cmx17775041791@163.com (M.C.); mabing@hfut.edu.cn (B.M.); haiyan@hfut.edu.cn (H.J.)
[2] Engineering Research Center of High-Performance Copper Alloy Materials and Processing, Ministry of Education, Hefei 230009, China; chench@hfut.edu.cn
[3] School of Physics, Hefei University of Technology, Hefei 230601, China
* Correspondence: yfzhang@hfut.edu.cn

Abstract: The effect of different precipitates and nanoparticles on the distribution of radiation-induced dislocation loops in V-4Cr-4Ti alloy and V-4Cr-4Ti-1.8Y-0.4Ti_3SiC_2 alloy were studied. Both alloys were irradiated with 60 keV deuterium, and the distribution of the dislocation loops was statistically analyzed using the transmission electron microscope (TEM) technique. The results indicated that platelet-like Ti(CNO) precipitates affect the dislocation distribution, in which a significantly reduced dislocation number density in the area within 20 nm of the interface was observed. This phenomenon is attributed to the strong compressive strain in the vertical interface direction at the precipitates/matrix interface. No significant effect on loop distribution was observed in the coherent TiC/matrix interface, which may result from the almost no strain interface. In addition, the uniform distribution of radiation-induced dislocation loops in equivalent crystal orientation was confirmed via the TEM images with multiple *g* vectors.

Keywords: vanadium alloy; irradiation; precipitate; dislocation loop; TEM

check for updates

Citation: Wang, J.; Chen, M.; Zhang, Y.; Ma, B.; Jiang, H.; Chen, C. Effect of Precipitates on Dislocation Loops in Vanadium Alloy After Irradiation with 60 keV Deuterium Ions at Room Temperature. *Metals* **2024**, *14*, 1435. https://doi.org/10.3390/met14121435

Academic Editor: Andrii Kostryzhev

Received: 11 November 2024
Revised: 11 December 2024
Accepted: 12 December 2024
Published: 14 December 2024

Copyright: © 2024 by the authors. Licensee MDPI, Basel, Switzerland. This article is an open access article distributed under the terms and conditions of the Creative Commons Attribution (CC BY) license (https://creativecommons.org/licenses/by/4.0/).

1. Introduction

Magnetic confinement fusion is currently the most promising controlled nuclear fusion method and has become the fundamental path of the highly anticipated International Thermonuclear Experimental Reactor (ITER) program. One of the key issues that nuclear fusion reactors need to address is how the structural materials of nuclear fusion reactors can have a suitable working life under high temperature and high-energy (~14 MeV) neutron irradiation. The current candidate fusion reactor structural materials mainly include Reduced Activation Ferritic/Martensitic (RAFM) steels, SiC/SiC composites and vanadium alloys [1]. Vanadium alloys have better high-temperature mechanical properties than RAFM steels, with an upper limit of 1023 K, and also offer better processing and connection properties than SiC/SiC composites. Moreover, vanadium alloy has the advantages of compatibility with liquid Li [1–3], low activation, low magnetism, low radiation swelling and ideal high-temperature mechanical properties [4–6], so vanadium (V) alloy is considered as one of the most potential candidates for the first-wall structural material. In the last century, the microstructure of V-based alloys after irradiation has been widely investigated, especially on V-4Cr-4Ti and modified V-4Cr-4Ti alloys. It has been found that the microstructure of the V-4Cr-4Ti alloy after irradiation is highly correlated with Ti(CNO) precipitates [7] and additional nanoparticles, such as Y_2O_3 [8].

During neutron and ion irradiation, various types of Ti(CNO) precipitates were observed in V-4Cr-4Ti alloys [9,10], such as plate-like, needle-like or cuboid [11,12]. The

composition, shapes and distribution of the precipitates will seriously affect the mechanical properties and irradiation properties of vanadium alloy due to the additional sink strength provided by the precipitates/matrix [13–15]. Jiang et al. reported that after sequential irradiation with He and H ions at a dose of 5×10^{16} ions/cm^2, followed by annealing at 873 K for 10 h, precipitates of the V-4Cr-4Ti alloy would affect the growth direction and size of helium bubbles, resulting in more severe hardening [16]. Ohnuki et al. found that the strain field of precipitated phases provides nucleation sites for voids [9]. Therefore, in order to study the influence of precipitates on the evolution of the microstructure after irradiation, it is very useful to form precipitates through annealing before irradiation.

The additional nanoparticles are believed to significantly affect the distribution of irradiation defects due to the strong sink strength of the nanoparticle/matrix interface [17–19]. As reported by Zhang et al., the irradiation hardening rate of the V-4Cr-4Ti-1.8Y-0.4Ti_3SiC_2 alloy with added nanoparticles was lower than that of the V-4Cr-4Ti alloy [20,21]. In addition, atomic calculation by Zhang et al. indicated that Y is more easily combined with O [22], and Luo et al. reported that adding 1 wt.% Y to V-4Cr-4Ti can inhibit the formation of Ti rich precipitates [23]. The most important thing is that the addition of Y can effectively control the influence of O on the microstructure evolution during irradiation [24,25]. Zhang et al. reported that Y existed in two forms in V-4Cr-4Ti before irradiation, Y_2O_3 and YVO_4. Meanwhile, the reduction of the size and density for dislocation induced by the addition of Y was observed after irradiation [26]. Therefore, it is worth investigating the impact of additional nanoparticles on the evolution of irradiation defects in V-based alloys.

However, an obvious issue is that the effect of Ti(CNO) and nanoparticles on the evolution of the defect may be different due to the different interface structures, especially on the evolution of radiation-induced dislocation loops. In this work, the V-4Cr-4Ti alloy prepared by vacuum melting after annealing and the V-4Cr-4Ti-1.8Y-0.4Ti_3SiC_2 alloy prepared by mechanical alloying had pre-existing precipitates before irradiation. These samples were then irradiated with 60 keV Deuterium (D) ions at room temperature. It is worth mentioning that the ion irradiation carried out at room temperature is to investigate the evolution of self-interstitial atoms, while the vacancy-type defect becomes more movable at high temperatures. Transmission electron microscopy was used to characterize the evolution of precipitates and dislocation loops in the irradiated samples. The influence of precipitates on the distribution of dislocation loops was analyzed.

2. Materials and Methods

2.1. Materials

In this study, two types of vanadium alloys were utilized. The first one is V−4Cr−4Ti, prepared using the vacuum arc remelting (VAR) technique and annealing at 1073 K for 10 h [27]. The other one is the V-4Cr-4Ti-1.8Y-0.4Ti_3SiC_2 alloy, prepared via mechanical alloying (MA) and hot isostatic pressing (HIP) [21]. The purity of the powder used in V-4Cr-4Ti-1.8Y-0.4Ti_3SiC_2 is 99.9% (V), 99.7% (Cr), 99.4% (Ti), 99.5% (Y) and analytical grade (Ti_3SiC_2). The chemical composition of two kinds of V-based alloys is listed in Table 1.

Table 1. Chemical composition of two kinds of V-based alloy (wt. %).

V-Based Alloy	Cr	Ti	Y	Zr	Si	C	O	N	V
V-4Cr-4Ti	4.48	3.92				0.022	0.01	0.025	Bal.
V-4Cr-4Ti-1.8Y-0.4Ti_3SiC_2	4.60	4.64	1.52	0.14	0.074	0.11	0.85	0.18	Bal.

2.2. Microstructure Characterization

Samples for transmission electron microscopy (TEM) characterization were prepared by using the twin-jet electropolishing method. Discs with a diameter of 3 mm were cut from both kinds of V-based alloys and mechanically thinned to around 80 μm. Then, the discs were thinned to 100 nm by twin-jet electropolished using a 15% volume fraction methanol sulfate solution at −25 °C. The voltage and current are 30 V and about 50 mA, respectively.

The TEM observation was carried out using a FEI Tecnai G2 F20 TEM operated at 200 kV. Foil thicknesses were estimated based on the number of thickness fringes and the effective excitation error [28].

2.3. Ion Irradiation

60 keV D irradiation was carried out at room temperature using the ion implanter at the Institute of Semiconductors, Chinese Academy of Science. The fluence was 2.2×10^{16} ions/cm^2. Standard TEM samples were used in ion irradiation. In order to avoid errors caused by beam heating, all samples were irradiated simultaneously in this study and placed alternately in the same holder. The depth profile of the displacement damage was calculated using SRIM 2008 software with the Quick Kinchin-Pease mode [29]. The displacement threshold energies of Ed1 = 40 eV for V, Ed2 = 40 eV for Cr and Ed3 = 30 eV for Ti were used [30], and the atomic density was set to 7.05×10^{22} atoms/cm^3. The depth profiles of displacement per atom (dpa) and implanted D ions are plotted in Figure 1. The calculations indicate that the maximum damage level of approximately 0.12 dpa (displacements per atom) is located at a depth of around 400 nm. The displacement depth and ion range are estimated to be less than 700 nm, and the maximum concentration of D content is 1.75 at.%.

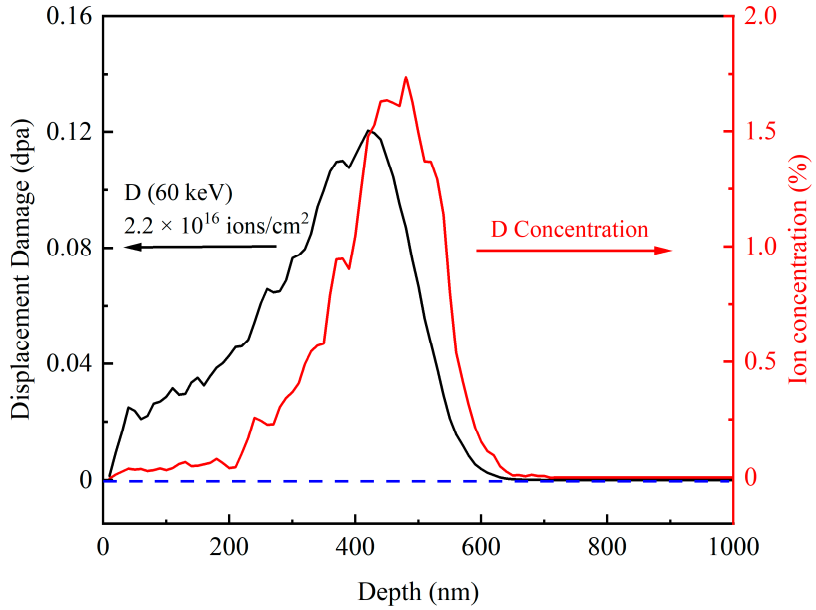


Figure 1. The depth profiles of the displacement damage and D concentration calculated using SRIM software.

3. Results

3.1. Microstructures Before Irradiation

Figure 2 shows the microstructure of V-4Cr-4Ti and V-4Cr-4Ti-1.8Y-0.4Ti_3SiC_2 alloys before irradiation. As shown in Figure 2a, the precipitates with a length of about 100 nm and a width of about 10 nm were observed in the V-4Cr-4Ti alloy. These precipitates were identified as having a Ti(CNO) structure, as shown in Figure 2b,c shows the particles and precipitates in V-4Cr-4Ti-1.8Y-0.4Ti_3SiC_2 alloy. Particles with different shapes were observed, as reported in previous research. These particles were Y_2TiO_7, TiC and Y_2O_3 [20]. Figure 2d shows the HRTEM image of a TiC nanoparticle with a size of about 10 nm. In addition, the similar platelet-like Ti(CNO) precipitates with a length of about 300 nm and a width of about 5 nm were observed and marked with blue arrows.

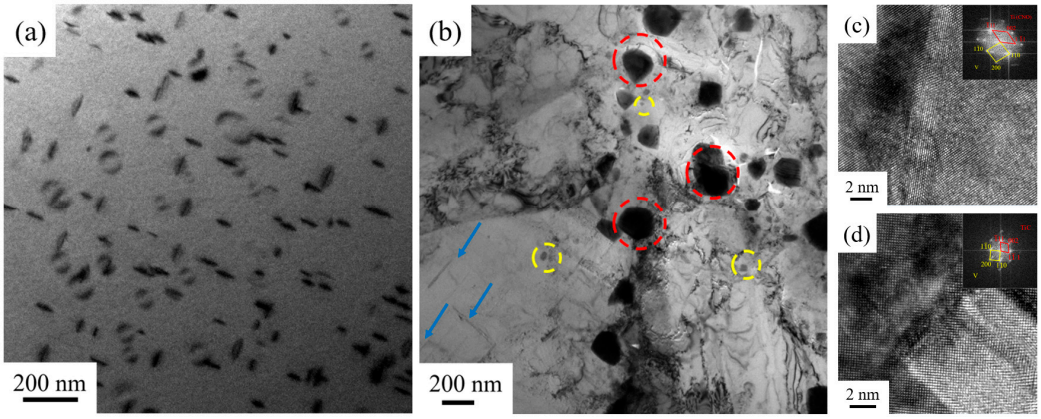


Figure 2. TEM images of precipitates in (**a**) V-4Cr-4Ti and (**b**) V-4Cr-4Ti-1.8Y-0.4Ti_3SiC_2 alloys before irradiation. (Red circle: large granular nanoparticles Y_2TiO_7; yellow circle: small granular nanoparticles TiC; blue arrow: platelet-like precipitates Ti(CNO)). (**c**,**d**): the HRTEM of platelet-like precipitates and granular nanoparticles.

3.2. Dislocation Distribution in D Irradiated V-4Cr-4Ti Alloy

Figure 3a shows the TEM bright field image of the dislocation loop near platelet-like precipitates in the V-4Cr-4Ti alloy after irradiation. The TEM images were recorded under the two-beam condition with g = (110). Figure 3b shows the enlarged images near a platelet-like precipitate. The statistical analysis of dislocation loops was carried out, in which the area used for statistics near the selected precipitate was divided into four regions, as shown in Figure 3b. The statistics will start from the distance of around 20 nm from the center of precipitates. The detailed statistical results are shown in Figure 4. Figure 4a–d show the distribution of dislocation loop size in four regions. Each region is a rectangle of the same size, with a length of 100 nm parallel to the precipitate and a width of 20 nm perpendicular to the precipitate. The number density and mean size of dislocation loops as a function of the distance from the precipitates are shown in Figure 4e. The number density of dislocation loops within the distance ranging from 0 to 20 nm is less than 5.0×10^{22} m^{-3}, which is significantly lower than that in further regions (approximately 9.0×10^{22} m^{-3}). In addition, no significant difference in the dislocation loop size was observed. The size of dislocation loops in all regions is about 3~4 nm. These results indicated that the dislocation loops are densely distributed near the platelet-like precipitates and tend to be uniform in further regions.

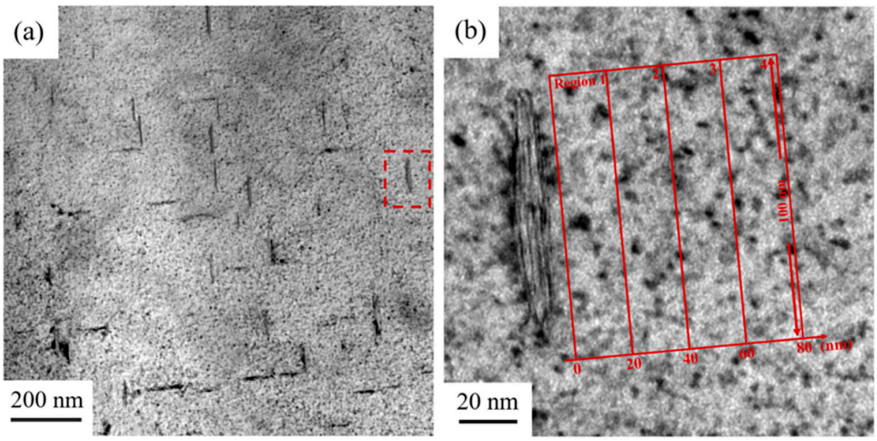


Figure 3. TEM bright field images of V-4Cr-4Ti alloy after irradiation. (**a**) TEM image of the distribution of larger precipitates and dislocation loops of V-4Cr-4Ti alloy after D-ion irradiation. (**b**) The enlarged TEM image of a selected precipitate, marked as a red box in (**a**).

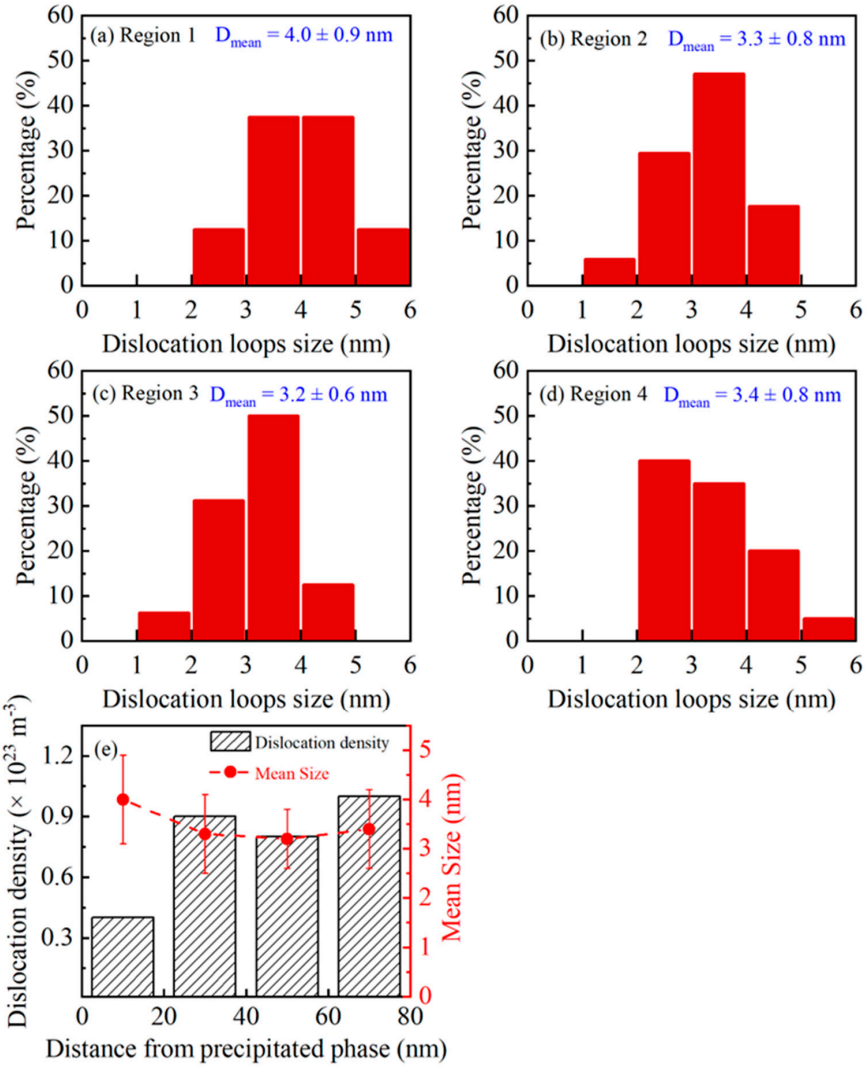


Figure 4. Statistical plots of the size and density distribution of the dislocation loops for the four regions in Figure 3b. Statistical distribution of dislocation loop size within the range of (**a**) 0–20 nm, (**b**) 20–40 nm, (**c**) 40–60 nm, and (**d**) 60–80 nm from the interface between the precipitates and the matrix; (**e**) Statistical distribution of dislocation loop size and number density within the range of 0–80 nm from the interface between the precipitates and the matrix.

Figure 5a shows the TEM bright field image of the dislocation loop near a smaller precipitate in the V-4Cr-4Ti alloy. The TEM images were recorded under the two-beam condition with g = (110). Figure 5b shows the enlarged image used in the statistical analysis of dislocation loops, in which the area used for statistics near the selected precipitate, as shown in Figure 5b. Four regions are divided starting from the precipitate's interface, with each region spaced every 20 nm. The results of dislocation loop size distribution are given in Figure 6. The number density and mean size of dislocation loops as a function of the distance from the precipitates are shown in Figure 6e. The dislocation loop density in region 1 is about 4×10^{22} m^{-3}, while it is almost twice (about 9×10^{22} m^{-3}) in further regions. In region 1, the average size of the dislocation loop is 3.0 ± 0.7, and no obvious change was observed in further regions. These observations indicate that the dislocation loops were influenced within a certain region near the Ti(CNO) precipitate in the V-4Cr-4Ti alloy.

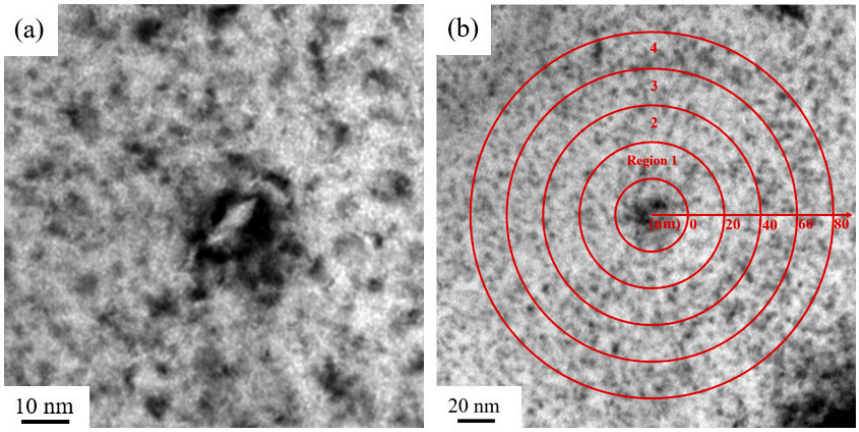


Figure 5. TEM images of (**a**) smaller precipitate and (**b**) dislocation loops of the V-4Cr-4Ti alloy after D-ion irradiation.

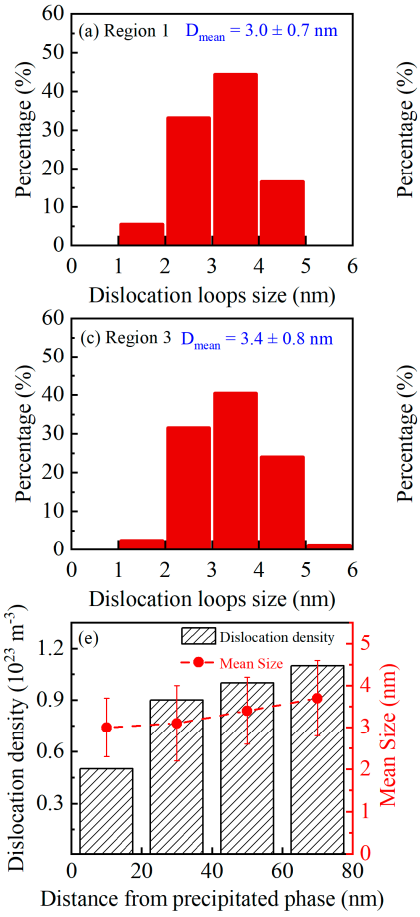


Figure 6. Statistical plots of the size and density distribution of the dislocation loops for the four regions in Figure 5b. Statistical distribution of dislocation loop size within the range of (**a**) 0–20 nm, (**b**) 20–40 nm, (**c**) 40–60 nm, and (**d**) 60–80 nm from the interface between the precipitates and the matrix; (**e**) Statistical distribution of dislocation loop size and number density within the range of 0–80 nm from the interface between the precipitates and the matrix.

3.3. Dislocation Distribution in D-Irradiated V-4Cr-4Ti-1.8Y-0.4Ti_3SiC_2 Alloy

Figure 7a shows the TEM bright field image of the dislocation loop near platelet-like Ti(CNO) precipitates in the V-4Cr-4Ti-1.8Y-0.4Ti_3SiC_2 alloy after irradiation. No significant change in the size of these precipitates was observed after irradiation. The number density and mean size of dislocation loops near a selected Ti(CNO) precipitate were statistically

analyzed. The counted area was divided into four regions, as shown in Figure 7b. The detailed results are shown in Figure 8a–d. The number density and mean size of dislocation loops as a function of the distance from the precipitates are shown in Figure 8e. The average size of the dislocation loops in the four regions is around 3.5 nm to 3.8 nm. No significant difference was observed. The number density of dislocation loops in region 1 was measured as 3×10^{22} m^{-3}, which is lower than that of other regions (about 5×10^{22} m^{-3}). This trend is consistent with Ti(CNO) precipitates in the V-4Cr-4Ti alloy.

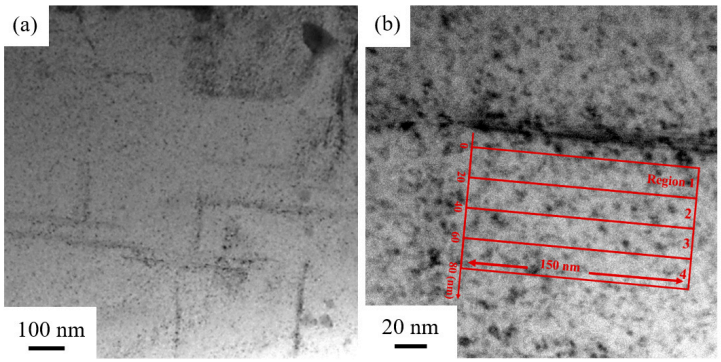


Figure 7. TEM images of (**a**) platelet-like precipitates and (**b**) dislocation loops of the V-4Cr-4Ti-1.8Y-0.4Ti_3SiC_2 alloy after D-ion irradiation.

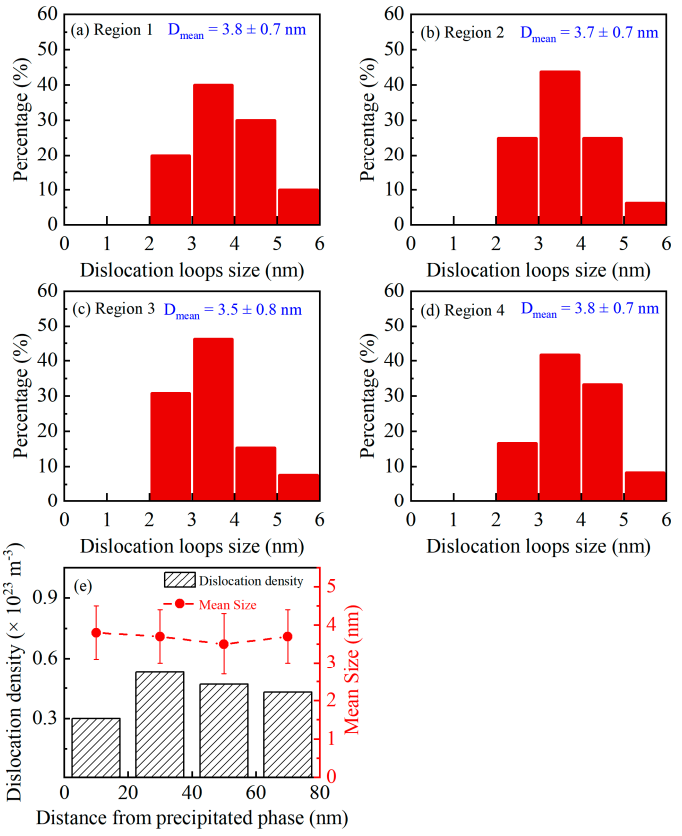


Figure 8. Statistical plots of the size and density distribution of the dislocation loops for the four regions in Figure 7b. Statistical distribution of dislocation loop size within the range of (**a**) 0–20 nm, (**b**) 20–40 nm, (**c**) 40–60 nm, and (**d**) 60–80 nm from the interface between the precipitates and the matrix; (**e**) Statistical distribution of dislocation loop size and number density within the range of 0–80 nm from the interface between the precipitates and the matrix.

The dislocation loops near a cubic nanoparticle are shown in Figure 9, where the low-magnification morphology is shown in Figure 9a, and the enlarged image near a

single particle is shown in Figure 9b. The distribution of dislocation loops was statistically analyzed, and the statistical regions were marked with red lines. The number density and mean size of dislocation loops as a function of the distance from the precipitates are shown in Figure 10. The average size of the dislocation loops in four regions is about 3.5 nm, and the number density is about 1.4×10^{23} m^{-3}. No significant difference in the number density and average size of dislocation loops was observed. This result is different from Ti(CNO) platelet-like precipitates, suggesting that the sink strength of nanoparticles seems to have no significant impact on the distribution of defects. The reason for this result will be discussed in Section 4.2.

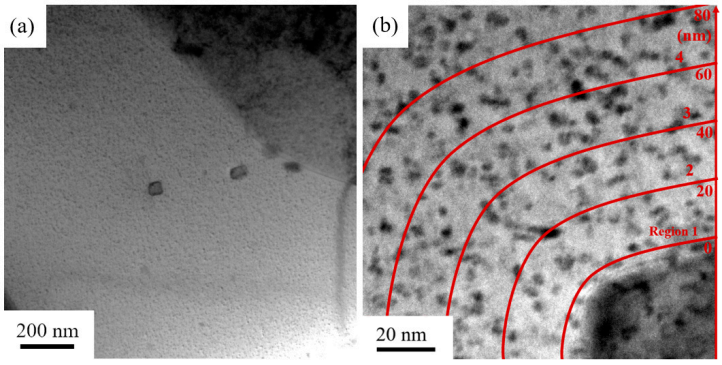


Figure 9. TEM images of (**a**) granular nanoparticles and (**b**) dislocation loops of V-4Cr-4Ti-1.8Y-0.4Ti_3SiC_2 alloy after D-ion irradiation.

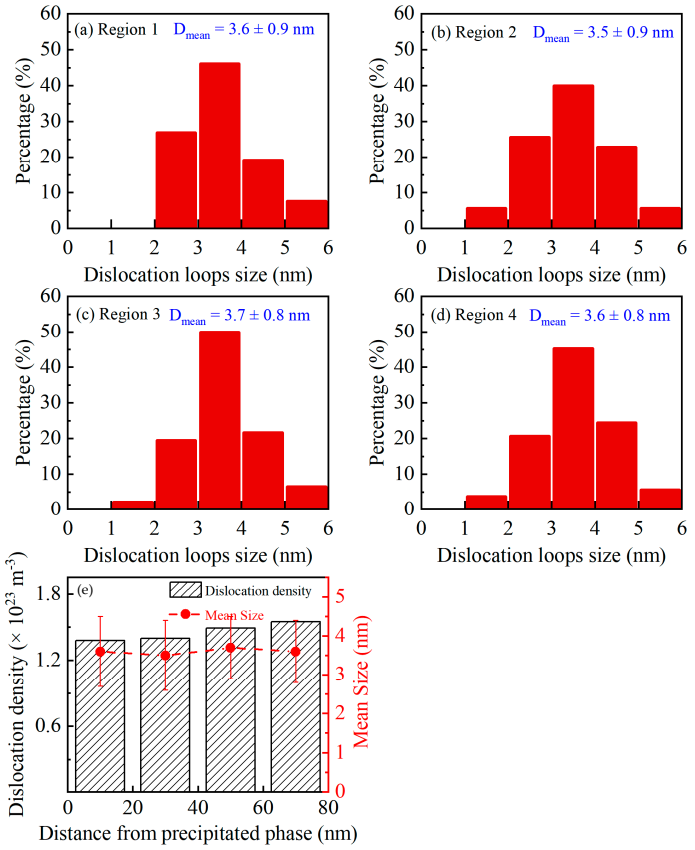


Figure 10. Statistical plots of the size and density distribution of the dislocation loops for the four regions in Figure 9b. Statistical distribution of dislocation loop size within the range of (**a**) 0–20 nm, (**b**) 20–40 nm, (**c**) 40–60 nm, and (**d**) 60–80 nm from the interface between the precipitates and the matrix; (**e**) Statistical distribution of dislocation loop size and number density within the range of 0–80 nm from the interface between the precipitates and the matrix.

4. Discussion

4.1. Types of Dislocation Loops After Irradiation

In the previous chapter, we made statistics on the distribution of dislocation loops near different precipitates after ion irradiation, but the premise of these statistical results is the uniform distribution of dislocation loops in equivalent crystal orientation. In this section, the dislocation loops were statistically analyzed using TEM under two-beam conditions with multiple g vectors, and the type and distribution of the dislocation loops were analyzed based on diffraction extinction. In this case, all the dislocations with the Burgers vector b that meet $g \cdot b = 0$ are not observed [31]. The statistical results of the dislocation loops are closely related to the selection of the g vector. If the dislocation loops are uniformly distributed in equivalent crystallography, the actual dislocation density can be estimated through a series of g-vector images. Therefore, the distribution of dislocation loops in equivalent crystal orientation is one of the key issues.

Figure 11 shows the dislocation loops of the V-4Cr-4Ti alloy in three different g vectors, where two equivalent g vectors, g_1 = (110) and g_2 = (101), as well as a non-equivalent g-vector, g_3 = (211) were selected. The observation area is in the vicinity of the same grain. The dislocation density of the V-4Cr-4Ti alloy under the g_3 = (211) vector is larger than that of the other two equivalent g-vectors. The size and density distribution of the dislocation loops in the V-4Cr-4Ti alloy captured under three g-vectors are shown in Figure 12. Under the two-beam condition, the size of dislocation loops captured in two equivalent g-vectors, g_1 = (110) and g_2 = (101), are 3.3 ± 0.7 nm and 3.4 ± 0.9 nm; the number densities are 0.9×10^{23} m^{-3} and 0.8×10^{23} m^{-3}. No significant difference in the size and number density of dislocations were observed under two equivalent g-vectors, indicating that the b-vector of dislocation loops is uniformly distributed in the equivalent crystallographic direction. The size and number density of dislocation loops captured in g_3 = (211) are 3.5 ± 0.9 nm and 1.3×10^{23} m^{-3}.

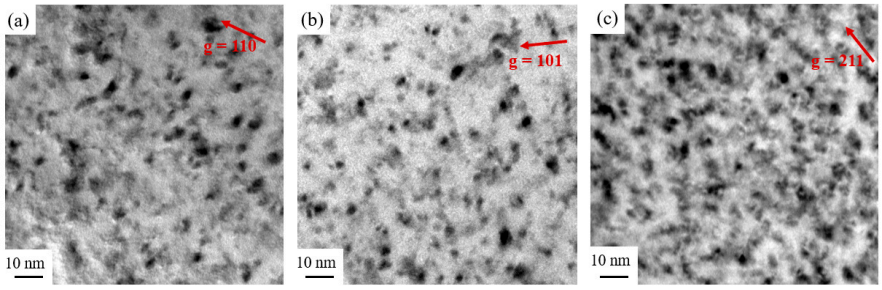


Figure 11. Dislocation loops of the V-4Cr-4Ti alloy under three different g-vectors after D-ion irradiation. ((**a**) g_1 = (110), (**b**) g_2 = (101) and (**c**) g_3 = (211)).

The types of dislocation loops in bcc-vanadium are different from those commonly found in general bcc metals, such as bcc-Fe and W. Cui et al. reported that the main types of radiation-induced dislocation loops in H-irradiated vanadium alloys at room temperature are the b = 1/2 < 111> and the b = <110> types [32,33]. The statistical dislocation extinction conditions are given in Table 2. The b = <110>-type loop under the g_1 = (110) vector has a 1/6 probability of diffraction extinction, and the b = 1/2 < 111>-type dislocations have a 1/2 probability of diffraction extinction. The b = <110>-type dislocations calculated under the g_3 = (211) vector have a 1/6 probability of diffraction extinction, and the mboxemphb = 1/2 < 111>-type dislocations have a 1/4 probability of diffraction extinction. Therefore, the proportion of the two types of dislocation loops can be estimated by Formulas (1) and (2).

$$\rho_{(g=(110))} = 5/6\rho_{(b=<110>)} + 1/2\rho_{(b=1/2<111>)} \quad (1)$$

$$\rho_{(g=(211))} = 5/6\rho_{(b=<110>)} + 3/4\rho_{(b=1/2<111>)} \quad (2)$$

where $\rho_{(g = (110))}$ represents the number density of dislocations counted under g_1 = (110), $\rho_{(g=(211))}$ represents the number density of dislocations counted under g_3 = (211), $\rho_{(b=<110>)}$ represents the number density of b = <110>-type dislocations, $\rho_{(b = 1/2<111>)}$ represents the number density of $b = 1/2 < 111>$-type dislocations.

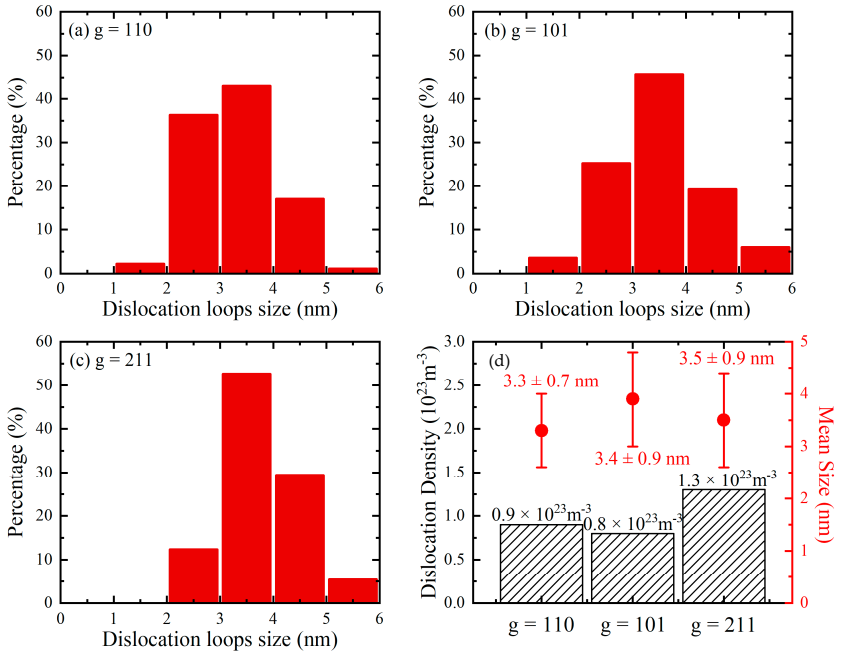


Figure 12. Statistical plots of the size and density distribution of the dislocation loops for three different g-vectors in Figure 11. The statistical distribution of dislocation loop sizes with g vectors of (**a**) g_1 = (110), (**b**) g_2 = (101) and (**c**) g_3 = (211); (**d**) The size and number density distribution of dislocation loops under three different g-vectors.

Table 2. Vanadium alloy diffraction extinction table.

$g\backslash b$	110	$\bar{1}10$	101	$\bar{1}01$	011	$0\bar{1}1$	111	$\bar{1}11$	$1\bar{1}1$	$11\bar{1}$
(110)	√	×	√	√	√	√	√	×	×	√
(211)	√	√	√	√	√	×	√	×	√	√

The actual dislocation density estimated under different g-vectors is shown in Table 3. The result shows that the dislocation loops produced by V-4Cr-4Ti alloy after D-ion irradiation are mainly $b = 1/2 < 111>$-type, with only a few b = <110>-type.

Table 3. The number density of dislocation loops in the V-4Cr-4Ti alloy.

Dislocation Loop	Dislocation Loops Under Different g-Vectors		Different Types of Dislocation Loops		Total
	g = (110)	g = (211)	b = <100>	b = ½<111>	
Number density/ $(10^{23}\mathrm{m}^3)$	0.9	1.3	0.1	1.6	1.7

4.2. Differences in Dislocation Loop Distribution at the Interface Between the Precipitates and the Matrix After Irradiation

The above results show that the b-vector of dislocation loops is uniformly distributed in the equivalent crystallographic direction. Therefore, it is reasonable to discuss the differences caused by precipitates in the distribution of dislocation loops.

The existing precipitates in vanadium alloys can influence the evolution of radiation-induced dislocation loops. The results in Figures 4, 6 and 8 show that the dislocation loop number density within 20 nm from the interface of platelet-like precipitates is relatively low and becomes uniform in further areas. This indicates that precipitates influence dislocation loop distribution only within the area 20 nm away from the interface of the precipitated phase.

It is common knowledge that the interaction between incident ions and atoms produces a rapidly moving primary knock-on atom (PKA). PKA will interact with other atoms in the lattice, forming a cascade collision, generating further displacement damage and producing some Frenkel defects (self-interstitial atoms/vacancy pairs). Then, most self-interstitial atoms (SIAs) and vacancies annihilate each other, while the remaining ones contribute to the formation of vacancy and self-interstitial clusters, such as dislocation loops [34,35]. Vacancies aggregate to form vacancy-type defects (such as void and vacancy-type dislocation loops), while SIAs aggregate to form interstitial defects (such as interstitial dislocation loops) [36]. In vanadium, the dislocation loops generated are mainly $1/2 < 111 >$-type vacancy dislocation loops and interstitial dislocation loops [33]. The formation and evolution of vacancies and SIAs are both influenced by lattice distortion caused by stress. In addition, research by Garner et al. [37,38] reported that due to the significant aggregation of point defects, the presence of external stress can lead to the anisotropic formation and growth of dislocation loops. Zhu et al. [39] obtained results using Molecular Dynamics (MD) simulation indicating that the presence of compressive stress reduces the energy required to form perfect dislocation loops, thereby promoting the formation of dislocation loops.

Figure 13 shows the HRTEM images and corresponding geometric phase analysis near the interface of platelet-like precipitates and TiC nanoparticles. For platelet-like precipitates, the [200] direction of the V matrix is selected as the x-direction, which is the growth direction of Ti(CNO) precipitates, and the [20] direction of the V matrix is selected as the y-direction. For TiC nanoparticles, the $[1\bar{1}0]$ and [110] directions of the V matrix are selected as x-direction and y-direction, respectively. The normal strain along the x-direction (ε_{xx}), y-direction (ε_{yy}), and the shear strain (ε_{xy}) are shown in Figure 13b,d. Interestingly, as shown in Figure 13b, a large compressive strain is observed along the y-direction (ε_{yy}) near the platelet-like precipitates, but no significant strain change occurs along the x-direction (ε_{xx}) and shear strain direction (ε_{xy}). Compared with platelet-like precipitates, Figure 13d shows that there is no obvious strain observed at the interface between granular nanoparticles and the matrix.

The difference in stress field may be the main reason for the difference in dislocation loop distribution. Due to the effect of strong compressive stress along the y-direction at the interface between the precipitates and the matrix, the growth of dislocation loops was promoted at the interface [39]. During the irradiation process, SIAs and vacancies generated near the platelet-like precipitated phase migrate to the interface. Due to the pinning effect of strain on the migrated SIAs and vacancies, their migration is hindered, and they aggregate at the interface to form a large number of dislocation loops. This pinning effect leads to a decrease in defect density near the interface, resulting in a decrease in dislocation loop density. This result can also be understood as the compressive stress along the y-direction of the platelet-like precipitate interface providing the driving force for the preferential nucleation and growth of dislocation loops at the interface between the precipitates and the matrix. This process reduces the concentration of point defects near region 1 (<20 nm), thus resulting in the low density of dislocation loops in region 1. The migration and aggregation of SIAs and vacancies at the interface between the precipitates and the matrix, as well as the preferential nucleation and growth of dislocation loops at the interface between the precipitates and the matrix, are fundamentally dependent on the effect of the stress. However, no such stress was observed at the interface between the granular nanoparticle and the matrix, so the distribution of dislocation loops at the interface of the granular nanoparticle is uniform.

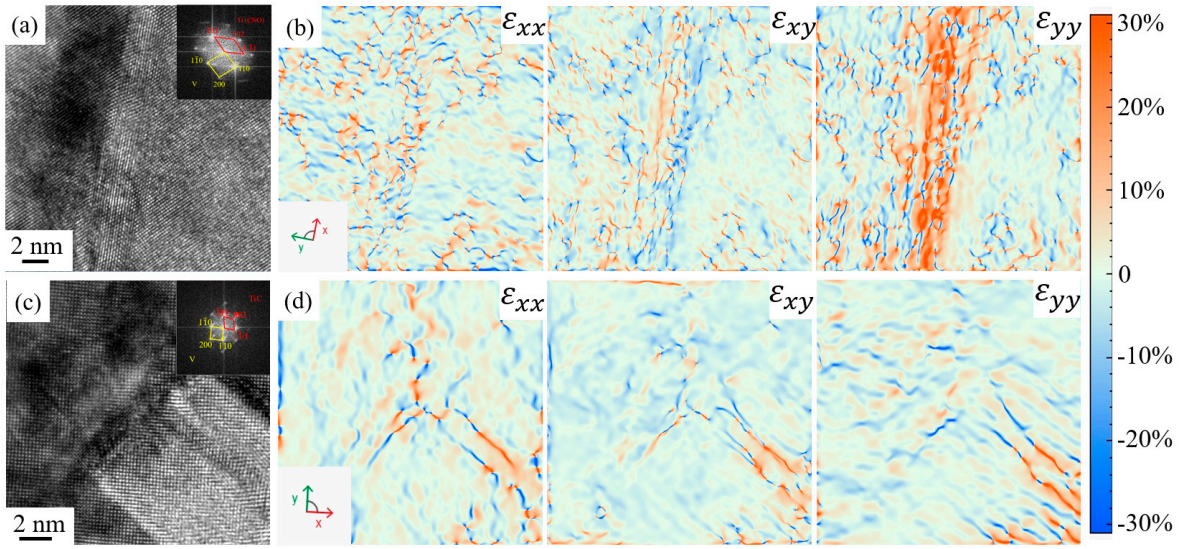


Figure 13. HRTEM images of (**a**) platelet-like precipitates and (**c**) granular nanoparticle. The GPA images obtained by the HRTEM images of (**b**) platelet-like precipitates and (**d**) granular nanoparticles.

In summary, due to the strong compressive strain in the vertical interface direction at the interface between platelet-like precipitates and the matrix, the formation of dislocation loops was promoted, leading to migration and enrichment of SIAs and vacancies towards the interface, ultimately suppressing dislocation formation near the interface. This phenomenon does not exist in granular nanoparticles due to the lack of significant strain at the interface.

5. Conclusions

In this work, the distribution of radiation-induced dislocation loops near different precipitates in the V-4Cr-4Ti alloy and the V-4Cr-4Ti-1.8Y-0.4Ti_3SiC_2 alloy were studied. The distribution of dislocation loops in equivalent crystal orientation and the effect of interface strain on the distribution of dislocation loops were discussed. Based on the results and analysis, the following conclusions can be drawn: The uniform distribution of radiation-induced dislocation loops in equivalent crystal orientation was confirmed in V-based alloy. The platelet-like Ti(CNO) precipitates affects the dislocation distribution due to the strong compressive strain in the vertical interface direction at the precipitates/matrix interface. This mechanism leads to a significantly reduced dislocation number density in the area within 20 nm of the interface but has no significant effect on further areas. No significant difference in dislocation distribution was observed near coherent TiC nanoparticles, which is attributed to the nearly strain-free interface.

Author Contributions: Writing—original draft preparation, J.W. and M.C.; investigation, M.C., H.J. and Y.Z.; writing—review and editing, Y.Z., J.W., B.M., H.J. and C.C.; project administration, J.W. All authors have read and agreed to the published version of the manuscript.

Funding: This work was supported by the Chinese National MCF Energy R&D Program (2022YFE03210200), the National Natural Science Foundation of China (12205070, 12205071), the Natural Science Foundation of Anhui Province (2308085ME134) and the Fundamental Research Funds for the Central Universities (PA2023GDSK0056 and JZ2023HGTB0213).

Data Availability Statement: The original contributions presented in this study are included in the article. Further inquiries can be directed to the corresponding author.

Conflicts of Interest: The authors declare no conflicts of interest.

References

1. Muroga, T.; Chen, J.; Chernov, V.M.; Kurtz, R.J.; Le Flem, M. Present status of vanadium alloys for fusion applications. *J. Nucl. Mater.* **2014**, *455*, 263–268. [CrossRef]
2. Chen, J.; Chernov, V.M.; Kurtz, R.J.; Muroga, T. Overview of the vanadium alloy researches for fusion reactors. *J. Nucl. Mater.* **2011**, *417*, 289–294. [CrossRef]
3. Smith, D.L.; Chung, H.M.; Loomis, B.A.; Matsui, H.; Votinov, S.; Van Witzenburg, W. Development of vanadium-base alloys for fusion first-wall-blanket applications. *Fusion Eng. Des.* **1995**, *29*, 399. [CrossRef]
4. Li, M.; Hoelzer, D.T.; Grossbeck, M.L.; Rowcliffe, A.F.; Zinkle, S.J.; Kurtz, R.J. Irradiation creep of the US Heat 832665 of V-4Cr-4Ti. *J. Nucl. Mater.* **2009**, *386*, 618–621. [CrossRef]
5. Zinkle, S.J.; Matsui, H.; Smith, D.L.; Rowcliffe, A.F.; Van Osch, E.; Abe, K.; Kazakovf, V.A. Research and development on vanadium alloys for fusion applications. *J. Nucl. Mater.* **1998**, *258–263*, 205–214. [CrossRef]
6. Smith, D.L.; Chung, H.M.; Loomis, B.A.; Tsai, H.C. Reference vanadium alloy V-4Cr-4Ti for fusion application. *J. Nucl. Mater.* **1996**, *233*, 356–363. [CrossRef]
7. Fukumoto, K.; Matsui, H.; Ohkubo, H.; Tang, Z.; Nagai, Y. Identification of ultra-fine Ti-rich precipitates in V-Cr-Ti alloys irradiated below 300 °C by using positron CDB technique. *J. Nucl. Mater.* **2008**, *373*, 289–294. [CrossRef]
8. Zhang, Y.; Sun, X.; Ma, B.; Wang, J.; Luo, L.; Wu, Y. Investigation of the Y Effect on the Microstructure Response and Radiation Hardening of PM V-4Cr-4Ti Alloys after Irradiation with D Ions. *Metals* **2023**, *13*, 541. [CrossRef]
9. Ohnuki, S.; Takahashi, H.; Kinoshita, H.; Nagasaki, R. Void formation and precipitation in neutron irradiated vanadium alloys. *J. Nucl. Mater.* **1988**, *155–157*, 935–939. [CrossRef]
10. Fukumoto, K.; Matsui, H.; Candra, Y.; Takahashi, K.; Sasanuma, H.; Nagata, S.; Takahiro, K. Radiation-induced precipitation in V-(Cr,Fe)-Ti alloys irradiated at low temperature with low dose during neutron or ion irradiation. *J. Nucl. Mater.* **2000**, *283–287*, 535–539. [CrossRef]
11. Impagnatiello, A.; Toyama, T.; Jimenez-Melero, E. Ti-rich precipitate evolution in vanadium-based alloys during annealing above 400 °C. *J. Nucl. Mater.* **2017**, *485*, 122–128. [CrossRef]
12. Zhu, B.; Yang, S.; Zhang, M.; Ding, J.; Long, Y.; Wan, F. Formation and evolution of platelet-like Ti-rich precipitates in the V-4Cr-4Ti alloy. *Mater. Charact.* **2016**, *111*, 60–66. [CrossRef]
13. Chung, H.; Loomis, B.A.; Smith, D.L. Effect of irradiation damage and helium on swelling and structure of vanadium-base alloys. *J. Nucl. Mater.* **1994**, *212–215*, 804–812. [CrossRef]
14. Jiang, S.; Wang, X.; Zhou, F.; Zhang, S.; Rao, W.; Wei, R.; Zheng, P. Effect of Ti-rich precipitation on mechanical properties of vanadium alloy after aging treatment. *Mater. Charact.* **2022**, *193*, 112320. [CrossRef]
15. Satou, M.; Abe, K.; Kayano, H. Tensile properties and microstructures of neutron irradiated V-Ti-Cr-Si type alloys. *J. Nucl. Mater.* **1994**, *212–215*, 794–798. [CrossRef]
16. Jiang, S.; Yang, C.; Zheng, P.; Guo, L.; Zhou, X.; Rao, W. Bubbles and precipitates formation and effects on the hardening of irradiated vanadium alloys. *J. Nucl. Mater.* **2021**, *544*, 152712. [CrossRef]
17. Šćepanović, M.; Leguey, T.; García-Cortés, I.; .Sánchez, F.J.; Hugenschmidt, C.; Auger, M.A.; De Castro, V. Sequential ion irradiations on Fe-Cr and ODS Fe-Cr alloys. *Nucl. Mater. Energy* **2020**, *25*, 100790. [CrossRef]
18. Zhou, Y.; Yin, S.; Zhou, Q.; Peng, J.; Luo, H.; Guo, L.; Li, H.; Yan, Y. Preliminary study on the microstructure and hardness of wire and arc additively manufactured ODS-RAFM steel subjected to 2.5 MeV Fe ion irradiation. *Nucl. Mater. Energy* **2023**, *36*, 101490. [CrossRef]
19. Duan, B.; Heintze, C.; Bergner, F.; Ulbricht, A.; Akhmadaliev, S.; Oñorbe, E.; De Carlan, Y.; Wang, T. The effect of the initial microstructure in terms of sink strength on the ion-irradiation-induced hardening of ODS alloys studied by nanoindentation. *J. Nucl. Mater.* **2017**, *495*, 118–127. [CrossRef]
20. Zhang, Y.; Du, J.; Liu, P.; Zheng, P.; Yang, S.; Wan, F.; Zhan, Q. Response of microstructure and hardening to deuterium ion irradiation in V-4Cr-4Ti-1.8Y-0.4Ti_3SiC_2 and V-4Cr-4Ti alloy. *Fusion Eng. Des.* **2020**, *159*, 111789. [CrossRef]
21. Wynne, B.P.; Gorley, M.J.; Zheng, P.; Cackett, A.J.; Porton, M.; Surrey, E. An analysis of the microstructure of spark plasma sintered and hot isostatically pressed V-4Cr-4Ti-1.8Y-0.4Ti_3SiC_2 alloy and its thermal stability. *J. Alloys Compd.* **2016**, *680*, 506–511. [CrossRef]
22. Zhang, P.; Li, X.; Zhao, J.; Zheng, P.; Chen, J. Atomic investigation of alloying Cr, Ti, Y additions in a grain boundary of vanadium. *J. Nucl. Mater.* **2016**, *468*, 147–152. [CrossRef]
23. Luo, H.; Luo, F.; Chen, Y.; Wang, J.; Liu, Q.; Li, F.; Xie, Z.; Lin, W.; Guo, L. Effect of yttrium content on microstructure and irradiation behavior of V-4Cr-4Ti-xY alloys. *J. Nucl. Mater.* **2022**, *559*, 153480. [CrossRef]
24. Watanabe, H.; Higashijima, A.; Yoshida, N.; Nagasaka, T.; Muroga, T. The microstructure of laser welded Y doped V-4Cr-4Ti alloys after ion irradiation. *J. Nucl. Mater.* **2009**, *386–388*, 598–601. [CrossRef]
25. Watanabe, H.; Yamasaki, K.; Higashijima, A.; Taguma, H.; Nagasaka, T.; Muroga, T. Microstructural changes of Y-doped V-4Cr-4Ti alloys after ion and neutron irradiation. *Nucl. Mater. Energy* **2016**, *9*, 447–450. [CrossRef]
26. Zhang, Y.; Li, R.; Diao, S.; Wan, F.; Zhan, Q. Plasticity improvement and radiation hardening reduction of Y doped V-4Cr-4Ti alloy. *J. Nucl. Mater.* **2022**, *560*, 153508. [CrossRef]
27. Ding, J.; Yang, S.; Zhu, B.; Liu, H.; Zhou, L.; Zhan, Q.; Wan, F. Twins induced by high-temperature ion irradiation in body-centered cubic V-4Cr-4Ti alloy. *Scripta Mater.* **2019**, *162*, 377–381. [CrossRef]

28. Hirsch, P.B.; Howie, A.; Pashley, D.W.; Whelan, M.J.; Marton, L. Electron Microscopy of Thin Crystals. *Phys. Today* **1966**, *19*, 93–95. [CrossRef]
29. Ziegler, J.F. *SRIM–The Stopping and Range of Ions in Matter, SRIM-2008.4*; SRIM: Annapolis, MD, USA, 1985.
30. *NRT ASTM E521*; Standard Practice for Neutron Radiation Damage Simulation by Charged-Particle Irradiation. ASTM International: Philadelphia, PA, USA, 1996.
31. Peng, B. The calculation of the extinction condition of crystal structure and its application. *J. Fushan Univ. (Nat. Sci. Ed.)* **2007**, *03*, 11–14. [CrossRef]
32. Cui, L.; Gao, J.; Du, Y.; Zhang, G.; Zhang, L.; Long, Y.; Yang, S.; Zhan, Q.; Wan, F. Characterization of dislocation loops in hydrogen-ion irradiated vanadium. *Acta Phys. Sin.* **2016**, *06*, 252–258. [CrossRef]
33. Qiu, R.; Chen, Y.; Gao, N.; He, X.; Dou, Y.; Yang, W.; Hu, W.; Deng, H. Molecular dynamics simulations of displacement cascades in vanadium: Generation and types of dislocation loops. *Nucl. Mater. Energy.* **2023**, *34*, 101394. [CrossRef]
34. Azevedo, C.R.F. A review on neutron-irradiation-induced hardening of metallic components. *Eng. Fail. Anal.* **2011**, *18*, 1921–1942. [CrossRef]
35. Gittus, J. *Irradiation Effects in Crystalline Solids*; Applied Science Publishers: London, UK, 1978.
36. Baluc, N. Material degradation under DEMO relevant neutron fluences. *Phys. Scripta* **2009**, *138*, 014004. [CrossRef]
37. Garner, F.A.; Wolfer, W.G.; Brager, H.R. A reassessment of the role of stress in development of radiation-induced microstructure. *J. ASTM Int.* **1978**, *24*, 694. [CrossRef]
38. Okamoto, P.R.; Harkness, S.D. Stress-biased loop nucleation in irradiated type 316 stainless steel. *J. Nucl. Mater.* **1973**, *48*, 204–206. [CrossRef]
39. Zhu, Z.; Qiu, R.; Chang, L.; Ma, G.; Deng, H.; Huang, H. The effect of stress state and He concentration on the dislocation loop evolution in Ni superalloy irradiated by Ni^+ & He^+ dual-beam ions: In-situ TEM observation and MD simulations. *J. Mater. Sci. Technol.* **2025**, *212*, 77–88. [CrossRef]

Disclaimer/Publisher's Note: The statements, opinions and data contained in all publications are solely those of the individual author(s) and contributor(s) and not of MDPI and/or the editor(s). MDPI and/or the editor(s) disclaim responsibility for any injury to people or property resulting from any ideas, methods, instructions or products referred to in the content.